Research Square

Preprints are preliminary reports that have not undergone peer review.
They should not be considered conclusive, used to inform clinical practice,
or referenced by the media as validated information.

Covalent stabilization of mutant p53 suppresses aggregation and restores apoptotic signaling

Jerson Silva

jerson@bioqmed.ufrj.br

Federal University of Rio de Janeiro https://orcid.org/0000-0001-9523-9441

Giulia Ferretti

Medical University of South Carolina https://orcid.org/0000-0002-1205-6090

Ruan Ribeiro

Federal Fluminense University

Mariana da Paz

D'Or Institute for Research and Education

Raissa dos Santos

Federal University of Rio de Janeiro

Francisca Guedes da Silva

Federal University of Rio de Janeiro

Gileno de Sousa

Federal University of Rio de Janeiro

Michelle Mota

Federal University of Rio de Janeiro

Julia Quarti

Federal University of Rio de Janeiro

Danilo Predes

Federal University of Rio de Janeiro

Beatriz Iandra

Oswaldo Cruz Foundation

Otacilio da Cruz Moreira

Oswaldo Cruz Foundation

Fernando da Silva

Federal Fluminense University

Vitor Ferreira

Federal Fluminense University

Luciana Rangel

Federal University of Rio de Janeiro

Article

Keywords:

Posted Date: August 12th, 2026

DOI: https://doi.org/10.21203/rs.3.rs-9073818/v1

License: This work is licensed under a Creative Commons Attribution 4.0 International License.
Read Full License

Additional Declarations: (Not answered)

Abstract

Missense mutations in TP53 frequently promote conformational destabilization and amyloid-like aggregation, contributing to tumor progression and resistance to therapy. Although mutant p53 aggregation has emerged as a potential therapeutic target, pharmacological strategies capable of directly suppressing this process remain limited. Here, we identify RCT-13 as an inhibitor of mutant p53 aggregation. In triple-negative breast cancer (TNBC) cells harboring the p53 R280K mutation, RCT-13 reduces intracellular aggregation, restores tumor-suppressive signaling, inhibits migration, and induces apoptosis in a p53-dependent manner. Mechanistically, biochemical and mass spectrometric analyses demonstrate that RCT-13 forms cysteine-dependent covalent adducts with the p53 core domain, preventing aggregation of the mutant protein in vitro. Importantly, treatment of xenograft tumors with RCT-13 reduces mutant p53 aggregation in vivo, as evidenced by decreased DO-1/A11 colocalization. Together, these findings establish covalent targeting of aggregation-prone cysteine residues as a strategy to suppress mutant p53 aggregation and restore apoptotic competence in cancer cells. Our results identify mutant p53 aggregation as a pharmacologically tractable vulnerability and support the development of covalent modulators of p53 conformation as potential therapeutic agents for p53-driven cancers.

Introduction

The tumor suppressor p53 plays a central role in maintaining genomic integrity by coordinating cellular responses to stress, including cell cycle arrest, DNA repair, senescence, and apoptosis. Through these mechanisms, p53 acts as a key barrier against malignant transformation and has therefore been termed the “guardian of the genome” [1,2]. Inactivation of the TP53 gene is one of the most common events in human cancer, occurring in more than half of all tumors [3,4].Unlike many other tumor suppressor genes that are usually inactivated by deletions or truncating mutations in cancers, *TP53* is predominantly altered by missense mutations that can lead to the expression of full-length mutant proteins (MT-p53) [5,6]. These mutant proteins not only lose canonical tumor suppressive functions but may also acquire oncogenic gain-of-function (GOF) activities that promote tumor progression, invasion, metastasis, and therapy resistance[7,8]

Several studies have demonstrated that many mutant p53 proteins undergo conformational destabilization, leading to misfolding and the formation of amyloid-like aggregates [9–11]. These aggregates can exert dominant-negative effects by sequestering wild-type p53 (WT-p53) and can also co-aggregate with other members of the p53 family, including p63 and p73, thereby amplifying oncogenic signaling [11,12]. Moreover, mutant p53 aggregates have been shown to propagate misfolded conformations in a prion-like manner, contributing to tumor heterogeneity and resistance to therapy [13,14]. Consistent with these observations, amyloid-like p53 aggregates have been detected in several tumor types [11,14].

The recognition that mutant p53 aggregation contributes to tumor biology has led to the emergence of therapeutic strategies aimed at targeting this process. Peptide-based inhibitors such as ReACp53 were among the first to demonstrate that aggregation-prone regions of mutant p53 can be targeted to disrupt amyloid formation and restore tumor-suppressive activity in cancer models [13]. In parallel, several small molecules have been reported to reactivate mutant p53 through covalent modification of cysteine residues within the DNA-binding domain. Notable examples include PRIMA-1 and its clinically investigated derivative APR-246 (Eprenetapopt), which are converted intracellularly into reactive electrophiles capable of modifying thiol groups and promoting conformational stabilization of mutant p53 [15–18]. Additional compounds, including PK11000 and MIRA-1, have also been shown to restore mutant p53 function through thiol-dependent mechanisms [19,20].

Despite these advances, the development of pharmacological strategies that directly suppress mutant p53 aggregation remains limited. In particular, it remains unclear whether covalent engagement of exposed cysteine residues within aggregation-prone conformations of the p53 DNA-binding domain can effectively stabilize mutant p53 and restore its tumor-suppressive functions in cellular and tumor contexts.

In breast cancer, TP53 mutations are particularly prevalent in triple-negative breast cancer (TNBC), a highly aggressive subtype that lacks effective targeted therapeutic options [21]. Among these mutations, the R280K variant, present in the widely used MDA-MB-231 cell line, is associated with conformational destabilization of the p53 core domain and an increased propensity to form amyloid-like aggregates. Consistent with this structural defect, mutant p53 R280K has been shown to promote gain-of-function phenotypes, including enhanced invasion, migration, and tumorigenicity [9,10,22].

In this study, we identify RCT 13, a menadione-derived small molecule, as a covalent modulator of mutant p53 aggregation. We demonstrate that RCT 13 directly engages cysteine residues within the p53 DNA-binding domain, suppressing aggregation and stabilizing a wild-type–like conformation and function. Using a combination of biophysical, cellular, and in vivo approaches, we demonstrate that RCT 13 reduces MT-p53 aggregation, reactivates tumor-suppressive programs, and induces apoptosis in triple-negative breast cancer models. Together, these findings establish a covalent stabilization of the aggregation-prone p53 core domain as a pharmacologically tractable strategy to restore apoptotic competence in mutant p53 driven cancers.

Results

RCT Compounds Reduce Viability of MDA MB 231 cells in a p53-Dependent Manner

A panel of synthetic naphthoquinone derivatives was screened for cytotoxic activity in breast cancer models (Supplementary Figs. 1 and 2). Among these, RCT 13 and RCT 14 emerged as the most promising candidates (Fig. 1a, Supplementary Fig. 1) and were selected for further cellular, *in vivo*, and *in vitro* characterization. To assess their effects on cell viability, two breast cancer cell lines were

employed: MDA MB 231, which harbors the R280K MT-p53, and MCF-7, which expresses WT-p53. The non-tumorigenic breast epithelial line MCF10A was included as a control for general cytotoxicity and selectivity index calculations.

To quantify cytotoxic potency and selectivity index, IC_{50} values were determined for RCT 13, RCT 14, menadione, and the reference compound PRIMA-1, a known modulator of MT-p53 aggregation [18,23]. Serial dilutions of each compound (menadione and RCTs, 0–50 μM; PRIMA-1, 0–400 μM) were tested for 72 h in MTT assays. As shown in Fig. 1b, both RCT 13 and RCT 14 were markedly more effective against MDA MB 231 cells than against MCF-7 or MCF10A, and exhibited higher potency and lower toxicity than PRIMA-1 or menadione.

Although RCT 13 and RCT 14 exhibited comparable cytotoxic activity in conventional 2D cultures, their effects diverged in a 3D spheroid model that more closely recapitulates tumor architecture. Under these conditions, RCT 13 produced a significantly greater reduction in MDA MB 231 viability than RCT 14 (Fig. 1c,d). This enhanced efficacy was accompanied by pronounced morphological alterations in the spheroids, including loss of spherical integrity and the emergence of a fragmented, crumbly appearance.

To determine whether the cytotoxicity of the compounds depends on p53 status, we used *TP53*-knockout MDA MB 231 cells generated by CRISPR-Cas9 (validated by western blot; Supplementary Fig. 2a). Cells were treated for 24 h with 10 μM doxorubicin (used as a TNBC reference drug), 50 and 100 μM PRIMA-1, 10 μM menadione, 10 μM RCT 13, or 10 μM RCT 14. As shown in Fig. 1c, deletion of p53 substantially diminished the cytotoxic effects of both RCT compounds relative to mock controls, suggesting that their activity is p53-dependent.

Collectively, these results indicate that RCT 13 and RCT 14 exert selective, p53-dependent cytotoxicity in breast cancer cells. Among them, RCT 13 stands out for its superior potency and efficacy in both 2D and 3D models, supporting its selection for subsequent mechanistic and *in vivo* analyses.

Mutant p53 R280K Reactivation and Functional Effects of RCT 13 and 14

Since the cytotoxic effect of RCT 13 and RCT 14 was reduced in p53 knockout cells, we investigated whether these compounds could also reactivate MT-p53, as previously shown for PRIMA-1 [16]. We performed immunofluorescence using the conformational antibody pAb1620, which specifically detects p53 in its wild-type conformation. MDA MB 231 cells, which express only the R280K mutant, were treated with 5 μM of each compound, and 50 μM of PRIMA-1 was included as a positive control (Supplementary Fig. 3).

Quantification by high-throughput screening (HTS) revealed that pAb1620 staining increased after treatment with RCT 13 (Fig. 2a,c), but not with RCT 14 (Fig. 2b). Because MDA MB 231 cells express only MT-p53, this increase in pAb1620 signal suggests that RCT 13 promotes a conformational shift toward a wild-type-like structure. Together with its p53-dependent cytotoxicity, these results suggest that RCT 13

promotes functional reactivation of MT-p53. In contrast, RCT 14 did not induce conformational reactivation, and its mechanism of action remains to be defined.

To determine whether the reactivation of MT-p53 by RCT 13 translated into functional restoration, we evaluated three canonical tumor-suppressive activities of WT-p53: inhibition of cell migration, induction of apoptosis, and activation of p53-responsive genes. In a wound-healing assay, MDA MB 231 cells were treated with 5 μM of each compound for 24 h in the presence of mitomycin C to block proliferation, ensuring that any observed effects were migration-specific. As shown in Fig. 2d, 2e, both RCT 13 and RCT 14 significantly reduced cell migration compared with the control.

We next assessed whether the compounds could trigger apoptosis, a well-established downstream outcome of functional p53 activation. MDA MB 231 cells were treated with 5 μM of each compound for 18 h and analyzed by annexin V/propidium iodide staining followed by flow cytometry (Fig. 2g). PRIMA-1 (50 μM) served as a positive control, given its known capacity to induce p53-dependent apoptosis (Supplementary Fig. 4b, c). As shown in the bar graphs, RCT 13 induced both early and late apoptosis at levels comparable to PRIMA-1, whereas RCT 14 induced a modest increase in early apoptosis.

To further probe the transcriptional response, we analyzed a panel of canonical p53 target genes (data not shown) and identified CDKN1A (p21) as the only transcript significantly upregulated by RCT 13 (Fig. 2h, i). A 4 h treatment increased p21 mRNA levels (Fig. 2h), and this induction was corroborated by immunoblotting after 24 h, which revealed cleaved p21(Fig. 2i), a form previously a form previously associated with apoptotic signaling [24]. These molecular findings are consistent with the annexin V/PI results.

Evaluation of the Potential of Selected Compounds to Modulate p53 R280K Aggregation

To examine whether RCT 13 and RCT 14 affect MT-p53 aggregation, we employed two complementary approaches. The first was the p53 Seprion-ELISA, which selectively detects amyloid-like aggregates through a high-molecular-weight polymer-coated matrix that captures aggregated proteins exceeding the size of oligomers. This method has been validated for distinguishing WT and MT-p53 aggregation states [25]. MDA MB 231 cells were treated with 5 μM or 10 μM of each compound for 18 hours, and total lysates (2 μg protein) were analyzed. Control groups included H1299 (p53-null) and MCF-7 (WT-p53) cells, which exhibited minimal signal, and MDA MB 231 cells treated with 50 μM PRIMA-1, previously shown to reduce MT-p53 aggregation [18]. These controls validated the specificity of the assay in our system.

As shown in Fig. 3a, RCT 13 treatment caused a dose-dependent reduction in p53 aggregation, whereas RCT 14 had no significant effect at either concentration. To confirm this finding, we conducted an independent aggregation assay based on immunoprecipitation with the anti-amyloid oligomer antibody A11. MDA MB 231 cells were treated with 10 μM of each compound, and 500 μg of total protein was subjected to immunoprecipitation. Western blot analysis of the precipitated fraction demonstrated that RCT 13 markedly decreased the amount of aggregated p53 (Fig. 3b,c), in agreement with the Seprion-ELISA results. No measurable change was observed with RCT 14 (Fig. 3b,d).

To further validate the reduction in intracellular aggregation, we performed confocal microscopy using co-staining with DO-1 (total p53) and A11 (amyloid-like aggregates) primary antibodies. In untreated MDA MB 231 cells, strong colocalization between DO-1 and A11 confirmed the presence of aggregated p53. Following treatment with RCT 13, colocalization was markedly decreased, consistent with reduced aggregation (Fig. 3e).

Together, these results demonstrate that RCT 13, but not RCT 14, markedly reduces mutant p53 aggregation in MDA MB 231 cells. This differential activity is consistant with an anti-aggregation mechanism for RCT 13, consistent with cysteine-dependent covalent engagement of mutant p53. In contrast, the lack of aggregation suppression by RCT 14 indicates that its effects on p53-associated phenotypes occur through an aggregation-independent mechanism. Importantly, suppression of MT-p53 aggregation by RCT 13 was accompanied by increased apoptotic signaling, suggesting that disruption of mutant p53 aggregates contributes to restoration of p53 dependent cell death pathways.

RCT 13 Reduces p53 Aggregation in tumors

To assess whether RCT 13 inhibits MT-p53 aggregation *in vivo*, we established a xenograft model using female athymic nude mice injected subcutaneously with MDA MB 231 cells, which express the R280K MT-p53. Once tumors reached a measurable size, animals were treated intraperitoneally with RCT 13, and tumor tissues were harvested for histological and molecular analysis.

Confocal microscopy of tumor sections was performed using dual immunostaining with DO-1, which detects total p53, and A11, an antibody that recognizes amyloid-like aggregates. Tumors from RCT 13-treated mice exhibited a marked reduction in p53 aggregation, as evidenced by decreased colocalization of DO-1 and A11 fluorescence signals (Fig. 4a,b). In contrast, vehicle-treated controls displayed strong and extensive overlap between these markers, indicating the persistence of aggregated MT-p53.

The reduction in DO-1/A11 colocalization provides *in vivo* evidence that RCT 13 suppresses MT-p53 aggregation within the tumor microenvironment. Importantly, this observation mirrors the effects observed in cell-based assays, supporting a mechanism consistent with aggregation suppression that extends to complex biological contexts. These data demonstrate that the compound maintains bioactivity under physiological conditions, suggesting intracellular engagement with its molecular target.

In addition to biochemical evidence of reduced aggregation, histological analysis of tumor tissues from nude mice revealed clear morphological alterations following RCT 13 treatment (Fig. 4b). Control tumors exhibited densely packed, disorganized cells infiltrating adjacent muscle fibers and displaying enlarged nuclei with prominent nucleoli, features characteristic of highly proliferative cancer cells. In contrast, tumors from RCT13–treated animals showed reduced cellular density, increased separation between stromal regions, and areas of nuclear condensation and cytoplasmic vacuolization. These features are suggestive of cell death by apoptosis or necrosis, although further quantitative analysis in larger cohorts will be required to substantiate these observations.

Liver tissue analyses showed RCT 13 treated mice have preserved hepatic architecture, with normal hepatocyte morphology and no signs of necrosis, vacuolization, or inflammatory infiltration (Fig. 4c). These findings are consistent with the absence of cytotoxic effects observed in non-tumorigenic MCF10A cells, suggesting that RCT 13 selectively targets cells under oncogenic or proteotoxic stress without causing detectable damage to normal tissues.

Together, these results demonstrate that RCT 13 reduces MT- p53 aggregation in tumors, providing in vivo validation of its anti-aggregation mechanism and supporting its translational potential as a small molecule that restores tumor-suppressive signaling by targeting the aggregation state of MT-p53.

RCT 13 Directly Interacts with the DNA-Binding Domain of the p53 R280K Mutant and Prevents Its Aggregation

To elucidate the molecular mechanism underlying the interaction of RCT 13 with the p53 R280K mutant, we first examined the direct binding of the compound to the purified DNA-binding domain (DBD) of p53. Intrinsic tryptophan fluorescence spectroscopy was used to monitor conformational changes upon ligand addition. The recombinant R280K DBD was incubated with increasing concentrations of RCT 13 (5 μM protein), and all samples were centrifuged and filtered (0.22 μm) to ensure the absence of pre-existing aggregates. RCT 13 caused a gradual, concentration-dependent decrease in fluorescence intensity without any shift in the emission maximum (Supplementary Fig. 4a,b). This quenching pattern is consistent with a direct interaction between the compound and the protein, with minimal perturbation of the tertiary structure. In contrast, RCT 14 induced a red shift in the emission spectrum and partial unfolding (Supplementary Fig. 4c–e), consistent with destabilization of the protein. Based on these results, subsequent mechanistic experiments focused exclusively on RCT 13.

To determine whether RCT 13 forms covalent adducts with the DBD, we performed mass spectrometry analysis of purified WT- and R280K-p53 DBD before and after compound exposure (Fig. 5a). Untreated proteins displayed masses consistent with their theoretical values, confirming sample integrity. Incubation with RCT 13 produced a clear mass shift for both WT and mutant DBDs, indicative of covalent modification. Pre-alkylation of free thiols with iodoacetamide generated the expected carbamidomethylation shift and completely abolished further mass changes upon subsequent RCT 13 incubation, demonstrating that the reaction is strictly thiol-dependent. These data support the formation of cysteine-dependent covalent adducts with both WT- and R280K-p53 DBDs.We next evaluated whether this interaction prevents aggregation of MT-p53 in vitro. Aggregation assays were performed under established conditions for p53 mutants [10,26–28]. Purified R280K DBD (5 μM) was incubated at 37°C for 2 h either alone or in the presence of 10 μM RCT 13. As shown in Fig. 5b, RCT 13 markedly reduced the light scattering signal, indicating a substantial inhibition of aggregation compared with the DMSO vehicle control. Fluorescence spectra recorded before and after incubation (Fig. 5c) revealed a subtle red shift following RCT 13 treatment, consistent with mild structural rearrangement rather than unfolding.

Collectively, these in vitro data indicate that RCT 13 directly and covalently engage cysteine residues within the DNA-binding domain of p53 R280K, stabilizing a native-like conformation and suppressing

aggregation. Although these experiments were performed using the isolated DNA-binding domain rather than full-length tetrameric p53, they provide mechanistic insight into the compound's mode of action and support a model in which covalent stabilization of the mutant core domain underlies the anti-aggregation and functional reactivation observed in cells and tumors.

Discussion

Missense mutations in *TP53* are among the most frequent genetic alterations in human cancers, occurring in over half of all solid tumors. Beyond loss of transcriptional activity, many of these mutations destabilize the DNA-binding domain, leading to extensive conformational rearrangements and misfolding into β-sheet–rich, amyloid-like structures[10,11]. Such aggregates impair tumor-suppressive functions while exerting dominant-negative and gain-of-function (GOF) effects [7,9]. Increasing evidence indicates that MT-p53 aggregates can display prion-like properties, propagating misfolding and sequestering WT-p53 as well as the related proteins p63 and p73 [9,10,29]. This process amplifies oncogenic signaling, disrupts apoptosis, and promotes genomic instability [30–33]. Clinically, p53 aggregation correlates with poor prognosis, metastasis, and therapy resistance in several cancers, including breast, ovarian, and glioblastoma [14,34,35]. Despite its biological significance, targeting MT-p53 aggregation remains largely unexplored as a therapeutic strategy.

A major goal of this study was to identify small molecules capable of disrupting MT-p53 aggregates, which are known to drive gain-of-function (GOF) oncogenic activities in various tumor models. These aggregates alter the transcriptional program of p53, promoting tumor progression, invasion, migration, and drug resistance [32,33,36–38]. Here, we identify RCT 13, a menadione-derived small molecule, as a covalent inhibitor of MT-p53 aggregation that restores wild-type-like structure and function. RCT 13 prevents aggregation of the p53 R280K mutant in vitro, reactivates p53-dependent transcriptional responses in breast cancer cells, and reduces MT-p53 aggregation in tumors. These finds indicates that a menadione derivative can engage and stabilize MT-p53 directly within the tumor microenvironment, validating MT-p53 aggregation as a druggable target.

Our biochemical and mass spectrometric analyses indicate that RCT 13 forms covalent adducts with cysteine residues in the DNA-binding domain of p53 R280K. Covalent modification of thiol groups is appears to be essential for activity, as pre-alkylation of cysteines abolished both binding and inhibition of aggregation (Fig. 5a). This cysteine-dependent mechanism resembles that of other small molecules—such as PRIMA-1, APR-246 (Eprenetapopt), MIRA-1, and PK11000—that refold MT-p53 through thiol reactivity. RCT 13 differs in exhibiting activity at lower effective concentrations, achieving aggregation inhibition in vivo, apparently without toxicity to normal cells. The contrasting behavior of the structurally related analog RCT 14, which destabilized p53, underscores how subtle chemical modifications can invert activity, highlighting the importance of fine-tuned structure–activity optimization.

The concept of targeting MT-p53 aggregation has only recently gained traction. Soragni and colleagues showed that the peptide ReACp53 disrupts aggregation-prone motifs and restores tumor-suppressive

function in an ovarian cancer model [13]. Although promising, peptide-based approaches face inherent challenges of stability and delivery. Natural polyphenols have also been shown to modulate p53 aggregation. In particular, resveratrol and its derivatives inhibit aggregation of both wild-type and mutant p53 in vitro and reduce amyloid-like p53 aggregates in breast cancer cells and xenograft tumors, as demonstrated by Ferraz da Costa et al. [39]. Although these compounds provide an important proof-of-concept that small molecules can target the aggregation pathway, their relatively low potency and limited chemical reactivity highlight the need for more robust and selective covalent modulators. More recently, Palanikumar et al. [40] described ADH-6, a tripyridylamide that prevents MT-p53 self-assembly and reactivates its transcriptional function. RCT 13 complements these advances through a distinct mechanism involving covalent thiol engagement rather than non-covalent steric inhibition — demonstrating that different chemical strategies can converge on the same oncogenic vulnerability. Another strategy to inhibit p53 aggregation involves the use of compounds based on thioflavin T (ThT)-like scaffolds [41]. These molecules often integrate multiple chemical moieties within a single framework, enabling multifunctional therapeutic approaches, such as simultaneous modulation of protein aggregation and chelation of Zn^{2+} ions [41,42]. Together, these efforts expand the chemical space for developing anti-aggregation therapeutics.

Functionally, RCT 13 restored key tumor-suppressive signalings of p53 in MDA MB 231 cells, including induction of apoptosis and inhibition of migration, thereby linking structural reactivation to biological outcome. The concomitant reduction of mutant p53 aggregates in xenograft tumors, evidenced by decreased DO-1/A11 colocalization, provides in vivo validation of this mechanism. Together, these findings support a model in which covalent engagement of cysteine residues within the p53 DNA-binding domain stabilizes conformational integrity, suppresses misfolding, and restores apoptotic competence in mutant p53–driven cancer cells (Fig. 6).Together, these findings support a model in which covalent engagement of cysteine residues within the p53 DNA-binding domain stabilizes conformational integrity, suppresses misfolding, and restores apoptotic competence in mutant p53–driven cancer cells, thereby linking structural reactivation to functional cell death pathways (Fig. 6).

Beyond establishing proof of concept, our results point to broader therapeutic and translational implications. Aggregation-targeted reactivation of p53 has the potential to enhance the efficacy of existing treatments, including chemotherapy and radiotherapy, by restoring apoptotic competence and counteracting mechanisms of chemoresistance that are closely associated with p53 aggregation in aggressive tumors. In this context, the recent detection of p53 aggregates in the plasma of glioma patients using ultrasensitive single-molecule assays provides evidence that p53 aggregation may represent not only a tumor-intrinsic phenomenon, but also a systemic and clinically measurable state [43]. These findings highlight the potential of aggregation- and conformation-sensitive biomarkers — such as A11 immunoreactivity, Seprion-ELISA, or emerging liquid biopsy – based assays — for patient stratification and longitudinal monitoring of therapeutic response.

Although the present work focuses on the R280K variant, a structural mutant associated with aggregation-prone behaviour, the underlying mechanism of covalent stabilization of the p53 DNA-binding domain may extend to other aggregation-prone *TP53* mutants. Future studies will be required to assess pharmacokinetics, tissue distribution, and efficacy across additional tumor models. Moreover, the menadione-derived scaffold described here provides a versatile starting point for structure-guided medicinal chemistry optimization, enabling the development of derivatives with improved selectivity, solubility, and bioavailability, as well as potential integration with biomarker-driven precision oncology strategies.

In conclusion, our study demonstrates that RCT 13 is a covalent small molecule capable of inhibiting mutant p53 aggregation and restoring tumor-suppressor function in vivo. Our findings provide experimental evidence that mutant p53 aggregation represents a pharmacologically tractable vulnerability and support covalent stabilization of the aggregation-prone core domain as an effective strategy for functional reactivation. Together with emerging aggregation-targeting approaches such as ADH-6 and ReACp53, our findings supports the view that p53 aggregation is not merely a pathological consequence of mutation, but a targetable Achilles' heel that can be exploited for the development of precision anticancer therapies.

Methods

Chemical synthesis of RCT 13 and RCT 14

The compound RCT 13 (2-(azidomethyl)-3-methyl-1,4-naphthoquinone) was prepared according to methodologies previously reported [44]. It was synthesized starting from 2-(chloromethyl)-3-methyl-1,4-naphthoquinone as follows. In a 25 mL round-bottom flask, 2-(chloromethyl)-3-methyl-1,4-naphthoquinone[45] (1 mmol, 0.220 g) and sodium azide (3 mmol, 0.195 g) were dissolved in aqueous solution (50%) of 10 mL of a 1:1 (v/v) mixture of distilled water and ethanol. The reaction mixture was subjected to ultrasonic irradiation for 30 min at room temperature. The mixture was extracted with ethyl acetate (3 × 20 mL). The combined organic phases were dried over anhydrous sodium sulfate, filtered, and concentrated under reduced pressure. The crude product was purified by silicagel column chromatography using a hexane/ethyl acetate gradient as eluent, affording the product RCT 13, which was obtained as an orange solid in 76% yield. The chemical structure of RCT 13 was unambiguously confirmed by spectroscopic and spectrometric analyses, including ^{1}H and ^{13}C nuclear magnetic resonance (NMR), infrared spectroscopy (IR), and high-resolution mass spectrometry (HRMS).

Melting point: 84–85°C. IR ν_{max} (cm^{-1}): 2174, 2092, 1659, 1624, 1591, 1443, 1381, 1331, 1290. ^{1}H NMR (500 MHz, DMSO-d6) δ (ppm): 8.04–7.96 (m, 2H), 7.88–7.81 (m, 2H), 4.42 (s, 2H), 2.18 (s, 3H). 13H NMR (125.00 MHz, DMSO-d6) δ (ppm): 184.3, 184.5, 146.3, 138.8, 134.0, 131.6, 131.0, 125.9, 125.8, 44.9, 12.6. HRMS (ESI^{+}): m/z $[M + Na]^{+}$ 250.0589 (calculated for $C_{12}H_9N_3NaO_2^{+}$: 250.0586).

RCT 14 (2-(((5H-[1,2,4]triazino[5,6-b]indol-3-yl)thio)methyl)-3-methyl-1,4-naphthoquinone) was synthesized using a thiol substitution strategy adapted from previously described methodologies for related compounds[46]. In a 50 mL round-bottom flask, 2-(chloromethyl)-3-methyl-1,4-naphthoquinone (1 mmol, 0.220 g), sodium hydroxide (1 mmol, 0.040 g), and distilled water (1 mL) were combined. To this mixture, 5H-[1,2,4]triazino[5,6-b]indol-3-thiol (1 mmol), previously solubilized in 2.5 mL of dimethyl sulfoxide (DMSO), was added dropwise. The reaction mixture was subjected to ultrasonic irradiation for 1 h at room temperature, leading to the formation of a precipitate. The solid was collected by vacuum filtration and further purified by silica gel column chromatography using a chloroform/methanol gradient as eluent. RCT 14 was obtained as a brown solid in 63% yield. Structural characterization was performed using ^{1}H and ^{13}C NMR (APT), Infrared Spectroscopy (IR), and high-resolution mass spectrometry (HRMS).

Melting point: 215–217°C. IR v_{max} (cm^{-1}): 1291, 1319,1335,1375, 1420, 1459, 1524, 1500, 1594, 1656, 1619, 2797, 2920, 3059. ^{1}H NMR (500 MHz, DMSO-d6) δ (ppm): 12.59 (s, 1H), 8.30 (d, J = 7.6 Hz, 1H), 8.05–8.02 (m, 1H), 8.01–7.98 (m, 1H), 7.88–7.80 (m, 2H), 7.69 (t, J = 7.6 Hz, 1H), 7.59 (d, J = 8.2 Hz, 1H), 7.43 (t, J = 7.5 Hz, 1H), 4.59 (s, 2H), 2.36 (s, 3H). ^{13}NMR (125.00 MHz, DMSO-d6) δ (ppm): 184.1, 183.1, 166.2, 146.4, 144.79, 141,5, 141.1, 140.3, 133.9, 133.8, 131.5, 131.3, 130.7, 125.9, 125.8, 122.3, 121.3, 117.5, 112.6, 25.9, 13.1. HRMS (ESI^{+}): m/z $[M + Na]^{+}$ 387.0927 (calculated for $C_{21}H_{15}N_4O_2SNa^{+}$: 387.0910).

A schematic overview of the synthetic routes for RCT 13 and RCT 14, including key intermediates and reaction conditions, is provided in Supplementary Fig. 1. All the data on chemical synthesis and characterization of RCT-13 and RCT-14 are provided in Table S1.

Cell culture

All cell cultures used in this work were obtained from the Rio de Janeiro Cell Bank (BCRJ, Brazil). The human breast epithelial tumor cell lines MCF-7 and MDA MB 231, and the non-tumorigenic epithelial line MCF10A, were cultured in high-glucose DMEM (Dulbecco's Modified Eagle's Medium – Cytiva, USA) supplemented with 10% fetal bovine serum (FBS) (Gibco®, USA). For MCF10A medium, mammary epithelial growth supplement (Thermo®, USA) was added. The cell lines were maintained at 37°C in a humidified atmosphere containing 5% CO_2. In addition, they were cultured in the presence of 10 µg/mL gentamicin.

Cell extracts and protein quantification

For the preparation of cell extracts, the culture medium was removed and the cells were trypsinized to maximize the yield of the process. The cells were then centrifuged at 1,000 × g for 5 minutes and washed three times with phosphate-buffered saline (PBS), alternating with centrifugations at 1,000 × g for 5 minutes, always at room temperature. After the last centrifugation, all the supernatant was discarded, and the lysis buffer containing (10 mM Tris-HCl, 150 mM NaCl, 1 mM EDTA, 1% Triton X-100

pH 7.5), and a protease inhibitor cocktail (Sigma-Aldrich, USA) was added to the pellet. Additionally, three cycles of freezing and thawing with liquid nitrogen were performed for physical lysis. Finally, the samples were centrifuged at 2,500 × g for 15 minutes at 4°C, and the supernatant was stored at − 20°C. The total protein concentration in the extracts was determined by the Lowry method [47], using 0.1% bovine serum albumin diluted in the same buffer as the samples as the standard.

Western Blotting

Equal amounts of cell extract samples (100 µg) were separated by electrophoresis on a 10% polyacrylamide gel (SDS-PAGE) (Laemmli, 1970). The proteins were then transferred onto a low-fluorescence polyvinylidene difluoride (PVDF) membrane (Immobilon® LF, Merck Millipore, USA). Membranes were blocked for 1 hour at 4°C in blocking buffer (Odyssey® Blocking Buffer – TBS, LI-COR Biotechnology, USA), and then incubated overnight at 4°C with the primary antibodies at a 1:1000 dilution. After incubation with the primary antibody, membranes were washed 5 times for 5 minutes with Tris-buffered saline containing (TBS-T), and incubated with secondary antibodies (anti-mouse or anti-rabbit) conjugated to IRDye® fluorophores (Red: IRDye® 680; Green: IRDye® 800CW – LI-COR Biotechnology, USA) for 2 hours at room temperature. Before detection, membranes were again washed 5 times with TBS-T. Fluorescent detection of the bands was performed using the Odyssey Infrared Imaging System (LI-COR Odyssey®, LI-COR Biotechnology, USA). β-actin levels were used as an internal control to verify equal protein loading. The following monoclonal primary antibodies were used: anti-p53 (mouse monoclonal, DO-1, Santa Cruz Biotechnology, USA, 1:1000), and anti-β-actin (mouse monoclonal, Sigma-Aldrich, USA, 1:10,000). Band quantification was determined by densitometric analysis using ImageJ version 1.43p (NIH, USA) and normalized to β-actin.

Co-Immunoprecipitation

For co-immunoprecipitation assays, 500 µg of total protein from cell lysates was brought to a final volume of 990 µL with PBS, and 10 µL of protease inhibitor cocktail were added. The samples were then incubated with 2 µg of the antibody of interest for 1 hour at 4°C under rotation. Next, 20 µL of protein A/G agarose resin (Santa Cruz Biotechnology, USA) were added and the samples were incubated overnight at 4°C under rotation. After incubation, the material was centrifuged at 1,000 × g for 5 minutes, and the supernatant discarded. The resin was then washed four times with 1 mL of cold PBS, centrifuging at 1,000 × g for 5 minutes between each wash. After the last wash, the supernatant was discarded and the beads were eluted with 40 µL of 1× sample buffer (50 mM Tris-Cl, pH 6.8, 2% SDS, 0.1% bromophenol blue, and 10% glycerol), followed by boiling for 3 minutes. The immunoprecipitated proteins were analyzed by SDS-PAGE (10%) and transferred to a low-fluorescence PVDF membrane. The subsequent procedures were the same as those described for the western blotting technique. In addition to the antibodies listed in section 3.4, the following were used: anti-amyloid oligomer antibody A11 (rabbit polyclonal, Millipore, USA), anti-p53 (rabbit polyclonal, Sigma-Aldrich, USA), and anti-IgG (mouse, Sigma-Aldrich, USA), which served as experimental control. Input samples, corresponding to 100 µg of total protein, were also used as internal controls.

p53 Seprion-ELISA

The reagents used in this experiment were from the Seprion-ELISA kit (MicrosensDX, England), which includes a 96-well detachable plate and a capture buffer [25]. A total of 2 µg of total protein from cell extracts (quantified as described previously) were diluted in PBS to a final volume of 100 µL and added to each well of the plate. Then, 25 µL of capture buffer were added to each well. After 100 minutes of incubation, five washes were performed with 0.1% Tween 20 in PBS. To determine whether the protein aggregates captured by the plate were p53, the anti-p53 DO-1 antibody was used at a 1:300 dilution. A total of 100 µL per well were added and incubated for 1 hour at room temperature, followed by three washes with 0.1% Tween 20 in PBS. To quantify the amount of captured p53 aggregates, an HRP-linked anti-mouse IgG secondary antibody (Santa Cruz Biotechnology, USA) was used at a 1:1000 dilution. A volume of 100 µL was added to each well and incubated for 45 minutes at room temperature. Finally, the plate was washed five times with 0.1% Tween 20 in PBS, and 100 µL of TMB substrate (Sigma-Aldrich, USA) were added to each well, followed by incubation for 25 minutes at room temperature. The reaction was stopped by adding 0.16 M sulfuric acid. Antibodies were diluted in a solution containing 0.1% Tween 20 in PBS, 4% serum albumin, 1% whole milk powder, and 0.15 M NaCl. The final absorbance was measured at 450 nm using a plate reader (SpectraMax® Paradigm®, Molecular Devices, USA), and the color intensity was correlated with the amount of aggregates captured in the wells.

MTT Cell Viability Assay

Cells from the different cell lines were seeded (5,000 cells) and cultured for 24 hours in 96-well plates, then treated with 10 µM of each of the 21 compounds, previously diluted in absolute dimethyl sulfoxide (DMSO) (Merck Millipore, USA), for 72 hours. Controls were performed by adding 0.01% DMSO to the culture medium. After the treatment period, the culture medium was removed, and 30 µL of MTT solution (0.5 mg/mL in PBS) were added to each well. The plates were incubated for 2 to 4 at 37°C in a 5% CO_2 atmosphere. Then, the formazan crystals were dissolved in 100 µL of DMSO. Cell viability was determined as the difference between absorbance at 570 nm and 650 nm, measured with a microplate reader, and expressed as a percentage relative to the DMSO control. The dose–response curve and IC_{50} value were calculated using GraphPad Prism 8.0 software.

Annexin V / Propidium Iodide Staining

To assess apoptosis-related biological events, the Annexin V/propidium iodide (PI) staining assay was performed. The protocol used in this experiment followed the manufacturer's instructions in the Dead Cell Apoptosis Kit with Annexin V-FITC and PI (Thermo Fisher, USA). Cells were cultured in 12-well plates until 80% confluence and treated for 18 hours with the compounds of interest. Cells were then detached using trypsin and resuspended in sterile PBS. The cells were centrifuged and resuspended in 1× Annexin V binding buffer provided in the kit. All samples were standardized to contain 1×10^6 cells/mL in 100 µL. To each sample, 5 µL of FITC–Annexin V and 1 µL of PI (stock solution 100 µg/mL) were added. Samples were incubated at room temperature for 15 minutes and resuspended in 400 µL of 1× binding

buffer. The samples were immediately analyzed on a flow cytometer (BD FACSVerse™). The fluorescence intensities of FITC–Annexin V and PI were detected at 530 nm and 575 nm, respectively.

Wound-Healing Assay

The migration activity of cells after treatment with the compounds was evaluated using the wound-healing assay. Cells were seeded in 24-well plates until 100% confluence. Using a sterile 200 µL pipette tip, a linear scratch (“wound”) was made in the center of the well, and the culture medium was replaced to remove detached cells. Fresh medium containing 10 µM of each compound and 0.01% DMSO as control was added. To ensure that the observed effects were due to migration rather than proliferation, mitomycin C (5 µg/mL), a DNA synthesis inhibitor, was included. Cells were treated for 24 hours, and images were taken at 0 and 24 hours using a bright-field microscope (EVOS™, Thermo Fisher) with a 10× objective. The wound width was measured using ImageJ software (version 1.43p, NIH, USA).

Purification of Recombinant p53 R280K (DNA Bind Domain)

The pET15b plasmid (Addgene, USA – #24866) containing the sequence encoding the central domain of MT-p53 R280K, inserted between the restriction sites NdeI and BamHI, was introduced into competent Escherichia coli BL21(DE3) cells by heat shock. Aliquots of 50 µL of competent cells were thawed on ice for 5 minutes, mixed with 2 µL of plasmid DNA (70 ng/µL), and incubated on ice for 30 minutes. Heat shock was performed at 42°C for 1 minute, followed by cooling on ice for 5 minutes. The cells were transferred to 1 mL of Luria–Bertani (LB) medium (Sigma-Aldrich, USA) and grown without selection at 37°C with constant shaking at 180 rpm. Cells were plated on solid LB agar (1% agar) containing 50 µg/mL ampicillin and incubated at 37°C for 18 hours to allow visualization of transformed bacterial colonies.

After transformation of the R280K mutant into E. coli BL21(DE3), expression began from a single colony inoculated into 25 mL of LB medium containing 50 µg/mL ampicillin. The culture was grown for 18 hours at 37°C and 180 rpm. Then, a 1:100 dilution of the culture was prepared in 800 mL of LB medium and grown at 37°C and 180 rpm until the optical density at 600 nm (OD_{600}) reached 1.2. At that point, protein expression was induced with 1 mM IPTG and continued for 18 hours at 15°C and 180 rpm. After induction, the cells were centrifuged at 10,000 × g for 20 minutes at 4°C.

The cell pellet obtained after centrifugation was resuspended in 30 mL of lysis buffer containing 50 mM Tris-Cl (pH 7.2), 50 mM NaCl, 2.5 mM DTT, and 1 mM PMSF (phenylmethylsulfonyl fluoride). Cells were lysed by sonication (Vibra Cell™, USA) for 30 minutes with 15-second pulses on/off at 13 watts, keeping the sample on ice throughout. The lysate was centrifuged at 20,000 × g for 15 minutes at 4°C (Hitachi Himac SCR20B). The supernatant was applied to a cation-exchange chromatography column (SP Sepharose; Amersham Pharmacia Biotech) pre-equilibrated with 50 mM Tris-Cl buffer (pH 7.2), 50 mM NaCl, and 2.5 mM DTT. The protein was eluted with a linear NaCl gradient from 50 mM to 400 mM in 3 mL fractions using an ÄKTA Purifier system (GE Healthcare, USA). The fractions corresponding to the main elution peak were diluted with Milli-Q water and applied to a heparin-affinity column (Heparin

Sepharose; Amersham Pharmacia Biotech). The protein was again eluted with a 50–400 mM NaCl gradient. Fractions corresponding to the elution peak were collected and dialyzed against 50 mM Tris-Cl buffer (pH 7.2), 150 mM NaCl, 5 mM DTT, and 5% glycerol. Protein concentration was determined spectrophotometrically using a molar extinction coefficient of 17,130 $M^{-1}cm^{-1}$ at 280 nm. Protein purity was confirmed by SDS-PAGE analysis and stored in liquid nitrogen.

Fluorescence Spectroscopy

To investigate conformational changes in protein structure and infer possible interactions with the selected compounds, fluorescence spectroscopy was performed. These experiments analyzed the aromatic amino acids tryptophan, tyrosine, and phenylalanine, which are intrinsic fluorophores used for monitoring protein structural changes. The fluorescence emission of these residues depends directly on the polarity of their environment. Thus, protein denaturation or dissociation processes can be monitored by shifts in the fluorescence emission spectrum. These shifts were quantified by calculating the spectral center of mass (<v>), which represents the average emission energy of the aromatic residues (MacGregor & Weber, 1986):

$$\langle v \rangle = \Sigma (v_i \times F_i) / \Sigma F_i$$

where F_i is the fluorescence intensity at each wavenumber v_i. When the aromatic residues are located in nonpolar environments (such as within folded proteins), emission occurs at shorter, more energetic wavelengths. Conversely, upon unfolding, the residues become exposed to solvent and emission shifts to longer wavelengths. The interaction assays between the compounds and the R280K mutant central domain were performed by monitoring fluorescence emission from the eight tyrosine residues of the protein, excited at 278 nm and collected from 295 to 415 nm. Samples were diluted to a final concentration of 5 µM in PBS buffer. Measurements were performed on an ISS/PC spectrofluorimeter (ISS Inc., USA) equipped with a 300 W xenon lamp and excitation/emission slit widths of 1 mm.

Light Scattering

To obtain information about particle size in solution, light scattering was measured at 90°. Measurements were performed using the same spectrofluorimeter described above.. Samples containing 5 µM of protein in the absence or presence of the compounds were excited at 320 nm, and scattered light was recorded between 300 and 340 nm. The ratio EL/EL_0 (scattered light / initial light) was used to determine the extent of aggregation under the experimental conditions. The wavelength of 320 nm was chosen because neither proteins nor nucleic acids absorb light at this wavelength[48]. To identify aggregate formation, light-scattering kinetics were recorded over 2 hours at 37°C, with excitation and detection both at 320 nm.

Generation of *TP53* knockout MDA MB 231 cells using CRISPR–Cas9

Knockout of TP53 in MDA MB 231 cells was achieved using the lentiCRISPRv2 vector (Addgene plasmid #52961), which encodes SpCas9 and a puromycin resistance cassette. Three single-guide RNAs (sgRNAs) were designed to target exons 5 and 6 of TP53 (gRNA1: 5'-CACCGCAGTCACAGCACATGACGG-3'; gRNA2: 5'-CACCGCAGCGCTCATGGTGGTGGTG-3'; gRNA3: 5'-CACCGCAGCTGGCAGGCTCCCGG-3'). Oligonucleotides were cloned into the BsmBI restriction site of the lentiCRISPRv2 plasmid following standard procedures. MDA MB 231 cells were transfected with each construct using Lipofectamine 3000 (Thermo Fisher Scientific) according to the manufacturer's instructions. After 48 h, cells were selected with puromycin (2 µg/mL) for 5 days to enrich for transfected populations. Single-cell clones were isolated by limiting dilution and expanded. Loss of p53 expression was confirmed by Western blot analysis in three independent clones. A mock control was generated by transfecting cells with the empty lentiCRISPRv2 vector lacking sgRNA sequences.

Mouse xenograft

All animal experiments were performed in accordance with the ethical guidelines established by the Brazilian National Council for the Control of Animal Experimentation (CONCEA) and were approved by the Institutional Animal Care and Use Committee (CEUA) of Federal University of Rio de Janeiro (Protocols 01200.001568/2013-87 and A09/24-013-20). Female athymic nude mice (6 weeks old) were maintained under pathogen-free conditions with free access to food and water. Subcutaneous xenografts were established by injecting 1 × 10^6 MDA MB 231 cells suspended in PBS into the right flank of each mouse. Once palpable tumors developed, animals were randomly assigned to treatment or vehicle groups. RCT 13 was administered intraperitoneally (2 mg/kg) for 20 days on a 5-days-on/5-days-off schedule. Control mice received DMSO + PBS using the same dosing regimen. At the end of treatment, tumors were harvested, fixed in 10% neutral-buffered formalin for 24 h, paraffin-embedded, and sectioned at 4 µm thickness. Tissue sections were stained with hematoxylin and eosin (H&E) for histopathological assessment, and additional sections were processed for immunofluorescence using antibodies against p53 (DO-1) and protein aggregates (A11). Images were acquired using identical exposure settings for all groups. Tumor size was not used as an endpoint, as this cohort was designed to investigate mechanistic effects of RCT 13 treatment rather than growth kinetics.

Mass spectrometry analysis of RCT 13 binding to p53 R280K

Recombinant human p53 DNA-binding domain (DBD, residues 94–312) containing either the wild-type or R280K (5 µM) was incubated with RCT 13 (10 µM) for 1 h at room temperature. Untreated samples were analyzed in parallel as controls. To determine whether RCT 13 interacts via cysteine residues, samples were pre-treated with iodoacetamide (IAA, 20 mM, 30 min, 25°C) to alkylate free thiols before addition of RCT 13. Reactions were quenched with 10 mM DTT, and proteins were desalted using Amicon Ultra centrifugal filters (10 kDa cutoff). Intact-protein mass spectrometry was performed on a Bruker ESI-QTOF mass spectrometer equipped with an electrospray ionization source, operated in positive ion mode. Spectra were acquired under standard intact-protein conditions and deconvoluted using Bruker Compass DataAnalysis to obtain zero-charge masses.

Statistical information

Results are expressed as mean ± standard error. Statistical analyses were performed using GraphPad Prism 7.0 software. Statistical comparisons between two groups were performed using Student`s t-test. Differences were considered statistically significant at $p \leq 0.05$.

Figure 1: **RCT-13 selectively reduces the viability of R280K mutant p53 breast cancer cells in a p53-dependent manner**. a, Chemical structures of RCT-13 and RCT-14. b, $IC_{50,}$ and Selectivity index for RCT-13, RCT-14, menadione, and PRIMA-1 in MDA-MB-231 (MT-p53 R280K), MCF-7 (WT-p53), and MCF-10A (non-tumorigenic). IC_{50} values were calculated after 72 h (MTT assay). c, Viability of mock versus TP53-knockout MDA-MB-231 cells treated for 24 h with the indicated compounds. Loss of p53 significantly reduces sensitivity to both RCT-13 and RCT-14. d, Representative bright-field images of 3D spheroids treated for 72 h with 5 μM RCT-13 or RCT-14, showing loss of compact architecture in RCT-13–treated spheroids. Scale bar, 200 μm. e, Quantification of spheroid viability after treatment. RCT-13 significantly reduces spheroid viability relative to RCT-14. Data are mean ± s.e.m.; Student's t-test; $p \leq 0.05$ considered significant. n = 3 independent experiments.

Figure 3: **RCT-13, but not RCT-14, decreases mutant p53 aggregation in cells.** a, p53 Seprion-ELISA quantification of aggregated p53 in MDA-MB-231 cells treated with 5 or 10 μM of each compound for 18 h. RCT-13 induces a dose-dependent decrease in aggregation; RCT-14 shows no effect. b, Western blot of A11-immunoprecipitated aggregates from cells treated with 10 μM RCT-13 or RCT-14. c,d, Densitometric quantification of aggregated p53 in A11-IP fractions showing a strong reduction with RCT-13 (c) and no change with RCT-14 (d). e, Confocal microscopy of MDA-MB-231 cells co-stained with DO-1 (total p53) and A11 (amyloid-like aggregates) showing markedly reduced DO-1/A11 colocalization after RCT-13 treatment. Scale bar, 10 μm. Data are mean ± s.e.m.; Student's t-test; $p \leq 0.05$. n = 3 biologically independent experiments.

Figure 4: **RCT-13 reduces mutant p53 aggregation in xenograft tumors in vivo.** a, Representative confocal images of xenograft tumor sections stained with DO-1 (total p53) and A11 (amyloid-like aggregates). RCT-13–treated tumors show reduced DO-1/A11 colocalization relative to vehicle controls, indicating decreased p53 aggregation. Scale bar, 20 μm. b, Representative H&E staining of tumor and liver sections. RCT-13–treated tumors show reduced cellular density and invasion compared with controls. c, Liver sections show preserved histological architecture, indicating the absence of detectable hepatotoxicity. Scale bar, 50 μm.

Figure 5: **RCT-13 covalently interacts with p53 R280K DBD and prevents its aggregation in vitro.** a, Intact-protein mass spectrometry of purified WT or R280K p53 DBD before and after incubation with RCT-13. A mass shift consistent with covalent adduct formation is observed. Pre-alkylation with iodoacetamide prevents RCT-13 binding, confirming thiol-dependent reactivity. b, Light-scattering kinetics of purified R280K DBD (5 μM) at 37°C for 2 h in the presence or absence of 10 μM RCT-13. RCT-13 markedly reduces scattering intensity, indicating potent inhibition of aggregation. c, Intrinsic fluorescence emission spectra of R280K DBD before and after incubation with RCT-13, showing minimal

spectral shift consistent with subtle conformational stabilization rather than unfolding. Data represent mean ± s.e.m. of n = 3 independent experiments.

Figure 6: **Covalent stabilization of mutant p53 by RCT-13 reverses amyloid aggregation and restores tumor suppression. a. The problem (mutant p53 aggregation).** The p53 R280K mutation results in an unfolded protein with exposed cysteine residues that assembles into amyloid-like fibrils (A11 positive). This aggregation drives gain-of-function (GOF) phenotypes, such as migration and invasion, and causes loss of function (LOF) due to a lack of transcriptional activity. **b. The mechanism (covalent targeting).** RCT-13 covalently binds to exposed cysteines on the unfolded mutant p53, stabilizing it into a folded, wild-type-like conformation recognized by pAb1620. The inactive analog, RCT-14, fails to bind and does not prevent aggregation. **c. The outcome (biological restoration).** (*Top panel*) Refolded p53 restores DNA binding and transcriptional activation of target genes like *p21* (mRNA), inducing apoptosis and inhibiting cell migration. (*Bottom panel*) In tumor xenografts, RCT-13 treatment significantly reduces A11-positive aggregates (red) relative to total p53 (green) compared to untreated controls, leading to tumor cell death and structural vacuolization.

Declarations

Ethics declarations

All animal procedures were approved by the Institutional Animal Care and Use Committee (IACUC) of

All animal procedures were performed in accordance with the ethical guidelines established by the Brazilian National Council for the Control of Animal Experimentation (CONCEA) and were approved by the Institutional Animal Care and Use Committee (CEUA) of Federal University of Rio de Janeiro under the protocol numbers 01200.001568/2013-87 and A09/24-013-20.

Competing Interest declaration

J.L.S., V.F.F, L.P.R, VFF, R.C.B.R., G.D.S.F., and F.C.S. are inventors on a patent application related to RCT-13 (Patent: Innovation Privilege. Registration number: BR1020230044891, Registration institution: INPI - Instituto Nacional da Propriedade Industrial - Deposited on March 10, 2023). The remaining authors declare no competing interests.

Funding

This work was supported by grants from the National Council for Scientific and Technological Development (CNPq), including the INCT program (grant nos. 465395/2014-7, 408046/2021-0, 408340/2024-0 to J.L.S.), by the Carlos Chagas Filho Foundation for Research Support of the State of Rio de Janeiro (FAPERJ) (grant nos. 210.008/2018, 202840/2018 and 210.776/2025 to J.L.S) and by the the Coordination for the Improvement of Higher Education Personnel (CAPES).

Data availability

All data supporting the findings of this study are available within the Article and its Supplementary Information. The Supplementary Information includes Supplementary Figures S1–S5 and Supplementary Table S1, which provide detailed chemical characterization of RCT-13 and RCT-14. Additional raw data are available from the corresponding authors upon reasonable request.

References

1. Lane DP. P53, Guardian of the Genome. *Nature* 1992; 358: 15–16.
2. Levine AJ. P53: 800 Million Years of Evolution and 40 Years of Discovery. *Nat Rev Cancer* 2020; 20: 471–480.
3. Olivier M, Hollstein M, Hainaut P. TP53 mutations in human cancers: origins, consequences, and clinical use. *Cold Spring Harb Perspect Biol* 2010; 2: 1–17.
4. Kandoth C, McLellan MD, Vandin F, Ye K, Niu B, Lu C *et al.* Mutational landscape and significance across 12 major cancer types. *Nature* 2013; 502: 333–339.
5. Brosh R, Rotter V. When mutants gain new powers: News from the mutant p53 field. *Nat Rev Cancer* 2009; 9: 701–713.
6. Muller PAJ, Vousden KH. Mutant p53 in cancer: New functions and therapeutic opportunities. *Cancer Cell* 2014; 25: 304–317.
7. Freed-Pastor WA, Prives C. Mutant p53: One name, many proteins. *Genes Dev* 2012; 26: 1268–1286.
8. Mantovani F, Collavin L, Del Sal G. Mutant p53 as a guardian of the cancer cell. *Cell Death Differ* 2019; 26: 199–212.
9. Xu J, Reumers J, Couceiro JR, De Smet F, Gallardo R, Rudyak S *et al.* Gain of function of mutant p53 by coaggregation with multiple tumor suppressors. *Nat Chem Biol* 2011; 7: 285–295.
10. Ano Bom APD, Rangel LP, Costa DCF, De Oliveira GAP, Sanches D, Braga CA *et al.* Mutant p53 aggregates into prion-like amyloid oligomers and fibrils: Implications for cancer. *J Biol Chem* 2012; 287: 28152–28162.
11. Silva JL, Gallo CVDM, Costa DCF, Rangel LP. Prion-like aggregation of mutant p53 in cancer. *Trends Biochem Sci* 2014; 39: 260–267.
12. Rangel LP, Costa DCF, Vieira TCRG, Silva JL. The aggregation of mutant p53 produces prion-like properties in cancer. *Prion* 2014; 8: 75–84.
13. Soragni A, Janzen DM, Johnson LM, Lindgren AG, Thai-Quynh Nguyen A, Tiourin E *et al.* A Designed Inhibitor of p53 Aggregation Rescues p53 Tumor Suppression in Ovarian Carcinomas. *Cancer Cell* 2016; 29: 90–103.
14. Yang-Hartwich Y, Soteras MG, Lin ZP, Holmberg J, Sumi N, Craveiro V *et al.* P53 Protein Aggregation Promotes Platinum Resistance in Ovarian Cancer. *Oncogene* 2015; 34: 3605–3616.

15. Bykov VJN, Issaeva N, Shilov A, Hultcrantz M, Pugacheva E, Chumakov P *et al.* Restoration of the tumor suppressor function to mutant p53 by a low-molecular-weight compound. *Nat Med* 2002; 8: 282–288.
16. Lambert JMR, Gorzov P, Veprintsev DB, Söderqvist M, Segerbäck D, Bergman J *et al.* PRIMA-1 Reactivates Mutant p53 by Covalent Binding to the Core Domain. *Cancer Cell* 2009; 15: 376–388.
17. Lehmann S, Bykov VJN, Ali D, Andreń O, Cherif H, Tidefelt U *et al.* Targeting p53 in vivo: A first-in-human study with p53-targeting compound APR-246 in refractory hematologic malignancies and prostate cancer. *J Clin Oncol* 2012; 30: 3633–3639.
18. Rangel LP, Ferretti GDS, Costa CL, Andrade SMMV, Carvalho RS, Costa DCF *et al.* P53 reactivation with induction of massive apoptosis-1 (PRIMA-1) inhibits amyloid aggregation of mutant p53 in cancer cells. *J Biol Chem* 2019; 294: 3670–3682.
19. Yu X, Vazquez A, Levine AJ, Carpizo DR. Allele-Specific p53 Mutant Reactivation. *Cancer Cell* 2012; 21: 614–625.
20. Bykov VJN, Issaeva N, Zache N, Shilov A, Hultcrantz M, Bergman J *et al.* Reactivation of mutant p53 and induction of apoptosis in human tumor cells by maleimide analogs. *J Biol Chem* 2005; 280: 30384–30391.
21. Koboldt DC, Fulton RS, McLellan MD, Schmidt H, Kalicki-Veizer J, McMichael JF *et al.* Cancer Genome Atlas Network. Comprehensive molecular portraits of human breast tumours. Nature. 2012;490(7418):61–70. doi:10.1038/nature11412. *Nature* 2012; 490: 61–70.
22. Silva JL, Gallo CVDM, Costa DCF, Rangel LP. Prion-like aggregation of mutant p53 in cancer. *Trends Biochem Sci* 2014; 39: 260–267.
23. Paz MM, Ferretti GDS, Martins-Dinis MMC, Ferreira BIS, Faier-Pereira A, Barnoud T *et al.* PRIMA-1 inhibits Y220C p53 amyloid aggregation and synergizes with cisplatin in hepatocellular carcinoma. *Front Mol Biosci* 2023; 10: 1–16.
24. Zhang Y, Fujita N, Tsuruo T. Caspase-mediated cleavage of p21(Waf1/Cip1) converts cancer cells from growth arrest to undergoing apoptosis. *Oncogene* 1999; 18: 1131–1138.
25. Maritschnegg E, Heinzl N, Wilson S, Deycmar S, Niebuhr M, Klameth L *et al.* Polymer-Ligand-Based ELISA for Robust, High-Throughput, Quantitative Detection of p53 Aggregates. *Anal Chem* 2018; 90: 13273–13279.
26. Bullock AN, Henckel J, Dedecker BS, Johnson CM, Nikolova P V., Proctor MR *et al.* Thermodynamic stability of wild-type and mutant p53 core domain. *Proc Natl Acad Sci U S A* 1997; 94: 14338–14342.
27. Ishimaru D, Andrade LR, Teixeira LSP, Quesado PA, Maiolino LM, Lopez PM *et al.* Fibrillar aggregates of the tumor suppressor p53 core domain. *Biochemistry* 2003; 42: 9022–9027.
28. Dos Santos NM, De Oliveira GAP, Rocha MR, Pedrote MM, Da Silva Ferretti GD, Rangel LP *et al.* Loss of the p53 transactivation domain results in high amyloid aggregation of the δ40p53 isoform in endometrial carcinoma cells. *J Biol Chem* 2019; 294: 9430–9439.
29. Petronilho EC, de Andrade GC, de Sousa G dos S, Almeida FP, Mota MF, Gomes AV dos S *et al.* Oncogenic p53 triggers amyloid aggregation of p63 and p73 liquid droplets. *Commun Chem* 2024; 7.

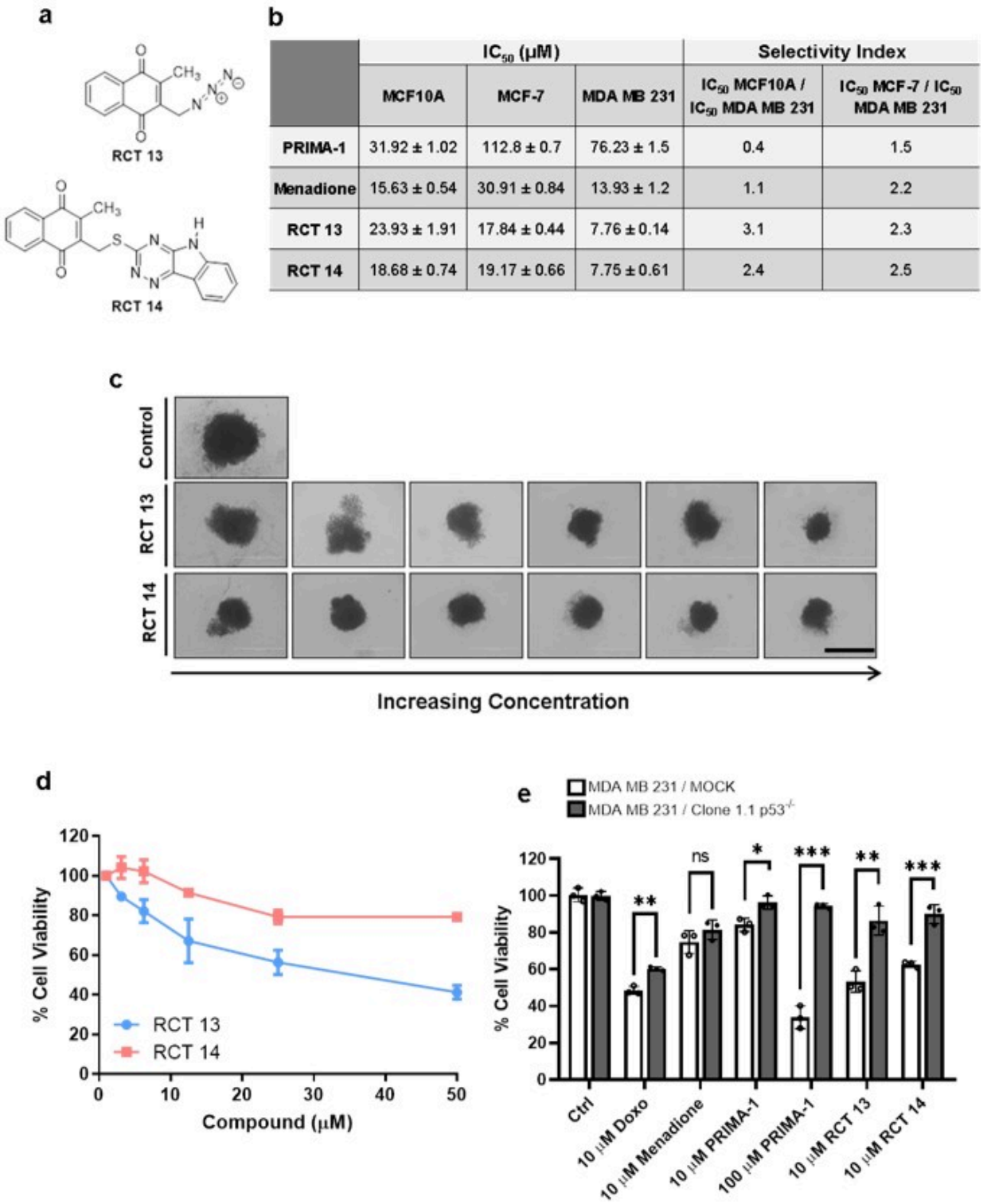
doi:10.1038/s42004-024-01289-x.

30. Petronilho EC, Pedrote MM, Marques MA, Passos YM, Mota MF, Jakobus B *et al.* Phase separation of p53 precedes aggregation and is affected by oncogenic mutations and ligands. *Chem Sci* 2021; 12: 7334–7349.
31. Adorno M, Cordenonsi M, Montagner M, Dupont S, Wong C, Hann B *et al.* A Mutant-p53/Smad Complex Opposes p63 to Empower TGFβ-Induced Metastasis. *Cell* 2009; 137: 87–98.
32. Muller PAJ, Caswell PT, Doyle B, Iwanicki MP, Tan EH, Karim S *et al.* Mutant p53 Drives Invasion by Promoting Integrin Recycling. *Cell* 2009; 139: 1327–1341.
33. Blandino G, Levine AJ, Oren M. Mutant p53 gain of function: Differential effects of different p53 mutants on resistance of cultured cells to chemotherapy. *Oncogene* 1999; 18: 477–485.
34. Levy CB, Stumbo AC, Ano Bom APD, Portari EA, Carneiro Y, Silva JL *et al.* Co-localization of mutant p53 and amyloid-like protein aggregates in breast tumors. *Int J Biochem Cell Biol* 2011; 43: 60–64.
35. Heinzl N, Koziel K, Maritschnegg E, Berger A, Pechriggl E, Fiegl H *et al.* A comparison of four technologies for detecting p53 aggregates in ovarian cancer. *Front Oncol* 2022; 12: 1–12.
36. Wong RPC, Tsang WP, Chau PY, Co NN, Tsang TY, Kwok TT. p53-R273H gains new function in induction of drug resistance through down-regulation of procaspase-3. *Mol Cancer Ther* 2007; 6: 1054–1061.
37. Schilling T, Kairat A, Melino G, Krammer PH, Stremmel W, Oren M *et al.* Interference with the p53 family network contributes to the gain of oncogenic function of mutant p53 in hepatocellular carcinoma. *Biochem Biophys Res Commun* 2010; 394: 817–823.
38. Pedrote MM, Motta MF, Ferretti GDS, Norberto DR, Spohr TCLS, Lima FRS *et al.* Oncogenic Gain of Function in Glioblastoma Is Linked to Mutant p53 Amyloid Oligomers. *iScience* 2020; 23: 100820.
39. da Costa DCF, Campos NPC, Santos RA, Guedes-da-Silva FH, Martins-Dinis MMDC, Zanphorlin L *et al.* Resveratrol prevents p53 aggregation in vitro and in breast cancer cells. *Oncotarget* 2018; 9: 29112–29122.
40. Palanikumar L, Karpauskaite L, Al-Sayegh M, Chehade I, Alam M, Hassan S *et al.* Protein mimetic amyloid inhibitor potently abrogates cancer-associated mutant p53 aggregation and restores tumor suppressor function. *Nat Commun* 2021; 12: 1–24.
41. Miller JJ, Blanchet A, Orvain C, Nouchikian L, Reviriot Y, Clarke RM *et al.* Bifunctional ligand design for modulating mutant p53 aggregation in cancer. *Chem Sci* 2019; 10: 10802–10814.
42. Miller JJ, Gaiddon C, Storr T. A balancing act: using small molecules for therapeutic intervention of the p53 pathway in cancer. *Chem Soc Rev* 2020; 49: 6995–7014.
43. Wu Y, Lam JYL, Pitoulias M, Böken D, Zhang Z, Chintapalli R *et al.* Detection of p53 aggregates in plasma of glioma patients. *Commun Med* 2025; 5. doi:10.1038/s43856-025-00918-3.
44. Silva JL Da, Silva FDC Da, Rangel LP, Ferreira VF, Sousa GDS De, Ferretti GDDS *et al.* NAFTOQUINONAS SINTÉTICAS E SEUS USOS NA PRODUÇÃO DE COMPOSIÇÕES FARMACÊUTICAS

COM PROPRIEDADES ANTITUMORAIS.
2025.https://patents.google.com/patent/BR122024022171A2/en.

45. Thomson RH. 240. Quinones. Part I. Chloroalkylation. *J Chem Soc* 1953;: 1196.
46. Zhang Q, Ding D, Zeng SX, Ye Q-Z, Lu H. Structure and Activity Analysis of Inauhzin Analogs as Novel Antitumor Compounds That Induce p53 and Inhibit Cell Growth. *PLoS One* 2012; 7: e46294.
47. Lowry O, Rosebrough N, Farr AL, Randall R. PROTEIN MEASUREMENT WITH THE FOLIN PHENOL REAGENT. *J Biol Chem* 1951; 193: 265–275.
48. Lakowicz JR. *Principles of fluorescence spectroscopy*. 2006 doi:10.1007/978-0-387-46312-4.

Figures



	IC_{50} (μM)			Selectivity Index	
	MCF10A	MCF-7	MDA MB 231	IC_{50} MCF10A / IC_{50} MDA MB 231	IC_{50} MCF-7 / IC_{50} MDA MB 231
PRIMA-1	31.92 ± 1.02	112.8 ± 0.7	76.23 ± 1.5	0.4	1.5
Menadione	15.63 ± 0.54	30.91 ± 0.84	13.93 ± 1.2	1.1	2.2
RCT 13	23.93 ± 1.91	17.84 ± 0.44	7.76 ± 0.14	3.1	2.3
RCT 14	18.68 ± 0.74	19.17 ± 0.66	7.75 ± 0.61	2.4	2.5

Figure 1

RCT-13 selectively reduces the viability of R280K mutant p53 breast cancer cells in a p53-dependent manner. a, Chemical structures of RCT-13 and RCT-14. b, $IC_{50,}$ and Selectivity index for RCT-13, RCT-14, menadione, and PRIMA-1 in MDA-MB-231 (MT-p53 R280K), MCF-7 (WT-p53), and MCF-10A (non-tumorigenic). IC_{50} values were calculated after 72 h (MTT assay). c, Viability of mock versus TP53-knockout MDA-MB-231 cells treated for 24 h with the indicated compounds. Loss of p53 significantly

reduces sensitivity to both RCT-13 and RCT-14. d, Representative bright-field images of 3D spheroids treated for 72 h with 5 µM RCT-13 or RCT-14, showing loss of compact architecture in RCT-13–treated spheroids. Scale bar, 200 µm. e, Quantification of spheroid viability after treatment. RCT-13 significantly reduces spheroid viability relative to RCT-14. Data are mean ± s.e.m.; Student's t-test; $p \leq 0.05$ considered significant. n = 3 independent experiments.

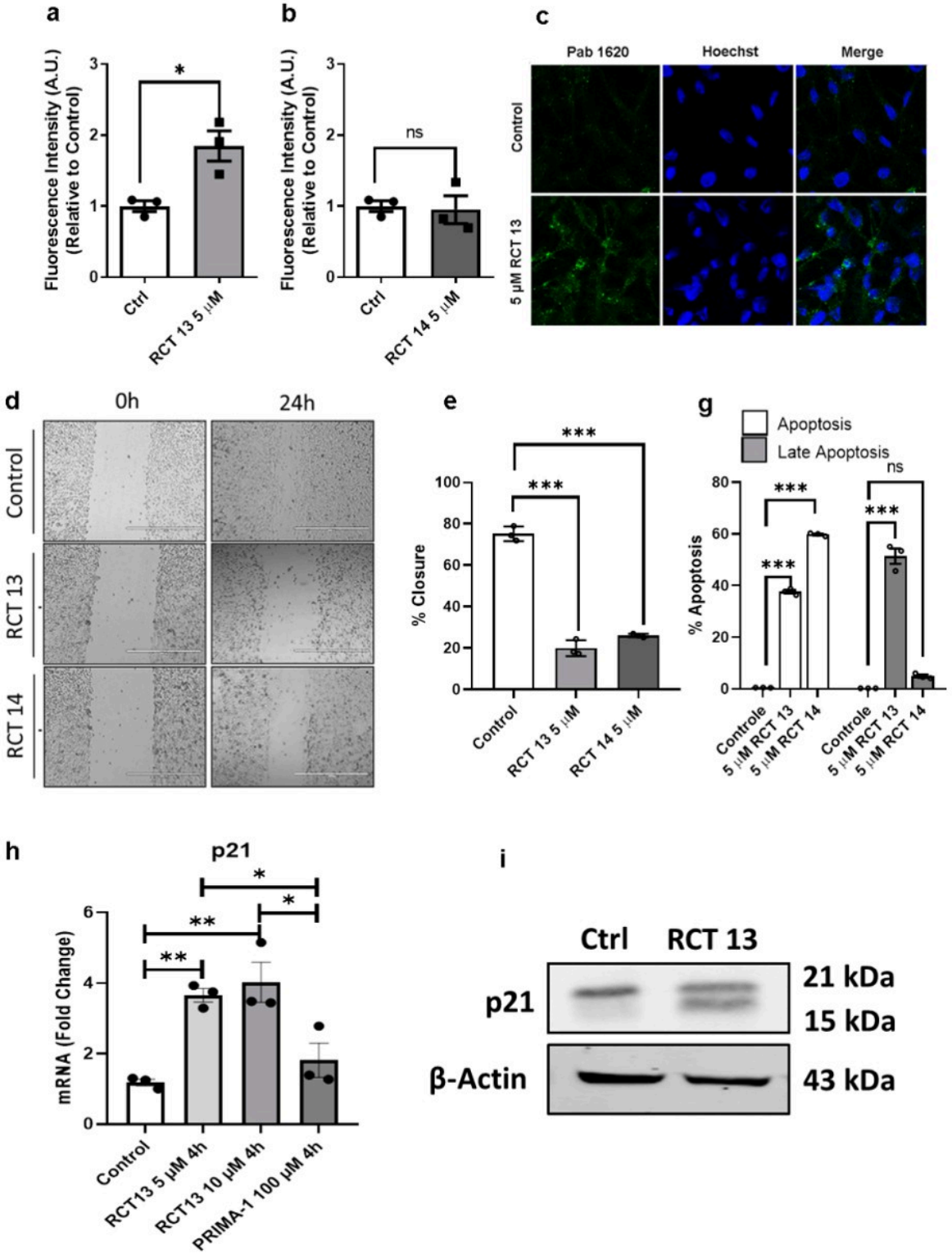


Figure 2

RCT-13 induces wild-type–like conformational reactivation of mutant p53 and restores tumor-suppressive functions. a-c, Immunofluorescence staining and quantification using the conformational antibody pAb1620 after 24 h treatment with 5 μM RCT-13 (a), RCT-14 (b) or DMSO. Representative images (c) show a significant increase in pAb1620 signal only with RCT-13, indicating acquisition of a WT-like conformation. Scale bar, 20 μm. d, Representative wound-healing images at 0 h and 24 h after treatment with the indicated compounds (5 μM) in the presence of mitomycin C. Scale bar, 200 μm. e, Quantification of wound closure showing reduced migration upon RCT-13 or RCT-14 treatment. g, annexin/Pi quantification. h, qPCR quantification of p21 after 4h of treatment. i, Western blot of p21 after treatment of MDA-MB-231 cells for 24 h with RCT-13, showing increased expression and appearance of cleaved p21 associated with apoptotic commitment. β-actin served as loading control. Data are mean ± s.e.m.; Student's t-test; $p \leq 0.05$. n = 3 independent experiments.

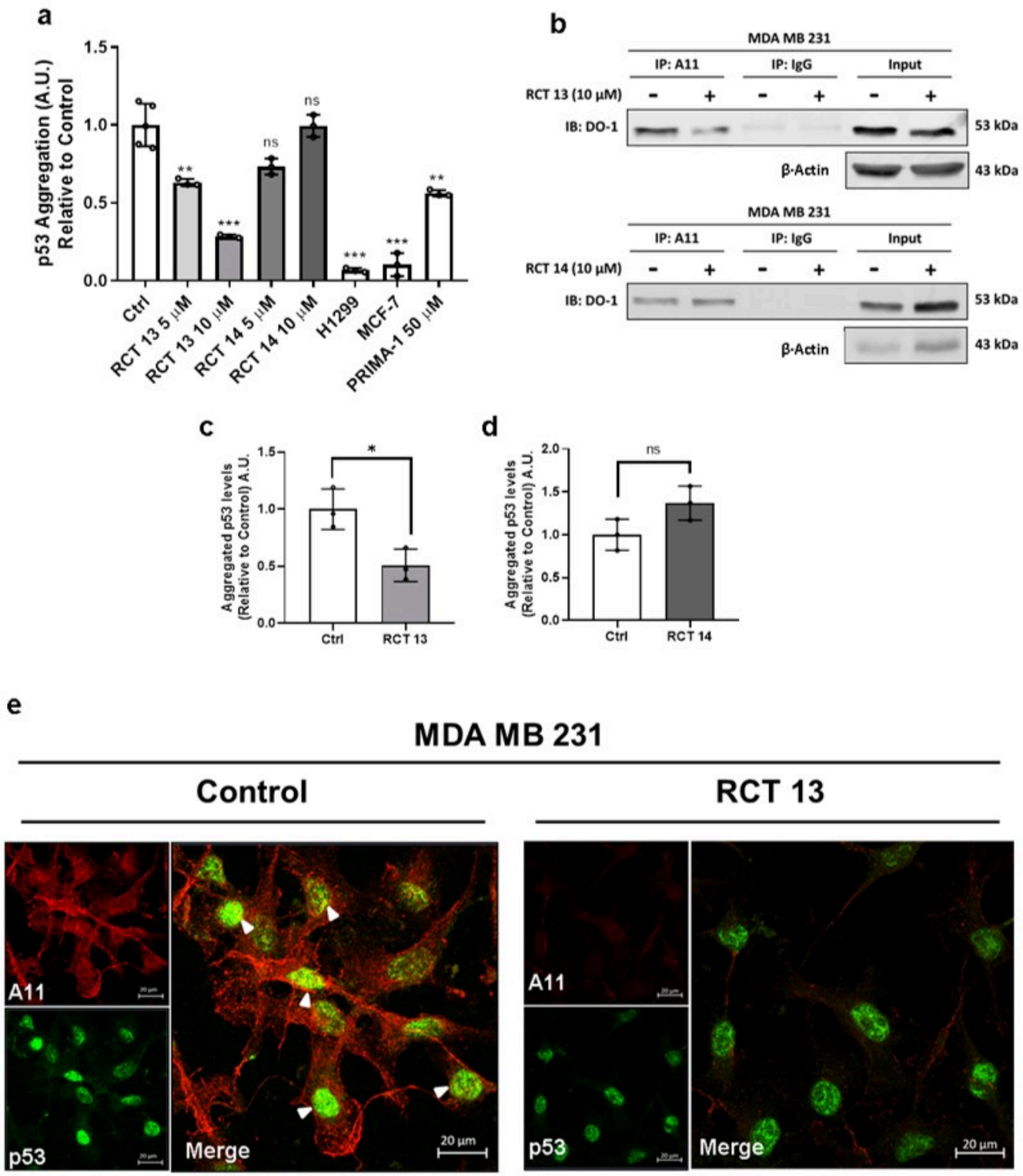


Figure 3

RCT-13, but not RCT-14, decreases mutant p53 aggregation in cells. a, p53 Seprion-ELISA quantification of aggregated p53 in MDA-MB-231 cells treated with 5 or 10 μM of each compound for 18 h. RCT-13 induces a dose-dependent decrease in aggregation; RCT-14 shows no effect. b, Western blot of A11-immunoprecipitated aggregates from cells treated with 10 μM RCT-13 or RCT-14. c,d, Densitometric quantification of aggregated p53 in A11-IP fractions showing a strong reduction with RCT-13 (c) and no

change with RCT-14 (d). e, Confocal microscopy of MDA-MB-231 cells co-stained with DO-1 (total p53) and A11 (amyloid-like aggregates) showing markedly reduced DO-1/A11 colocalization after RCT-13 treatment. Scale bar, 10 μm. Data are mean ± s.e.m.; Student's t-test; $p \leq 0.05$. n = 3 biologically independent experiments.

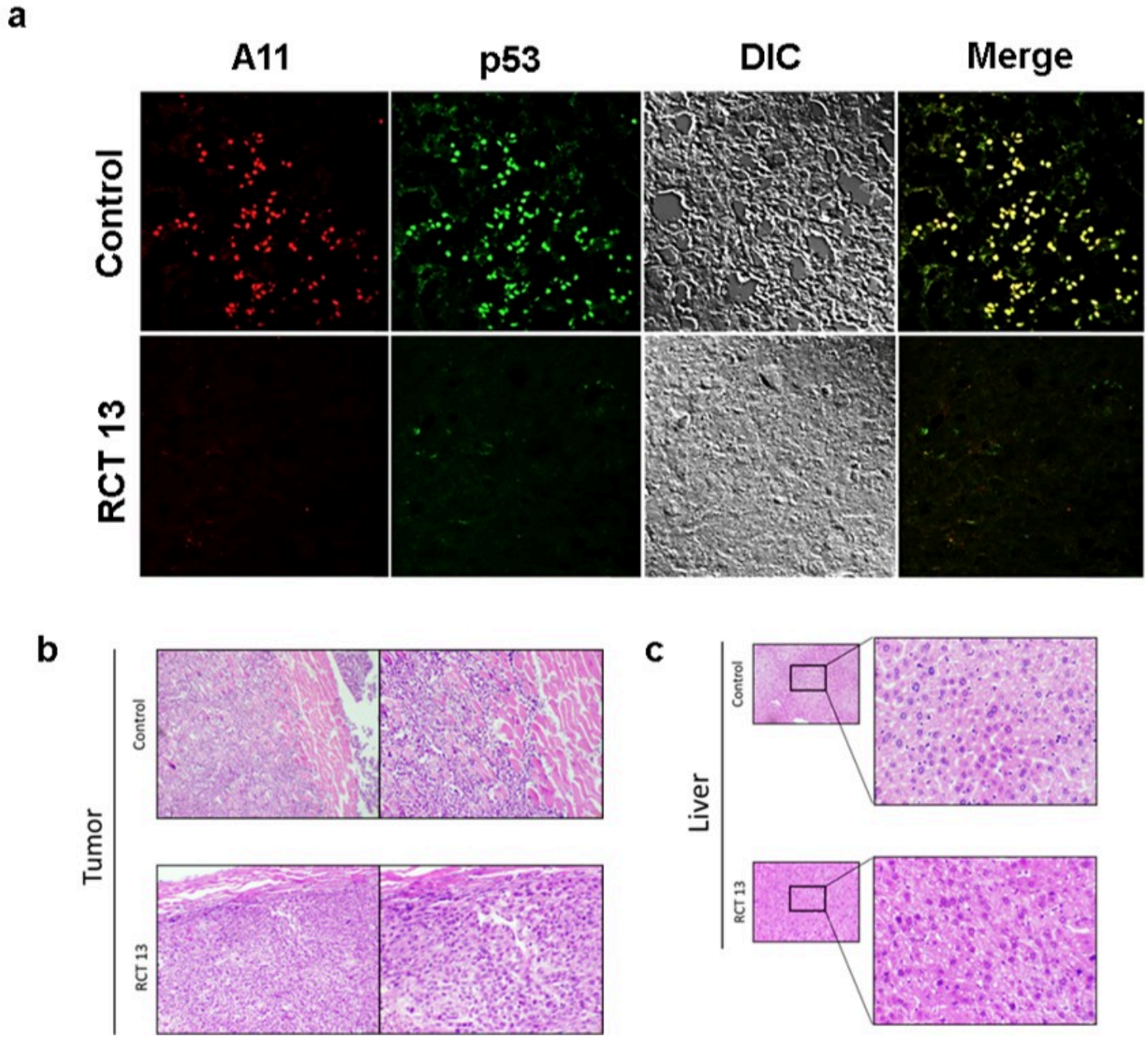
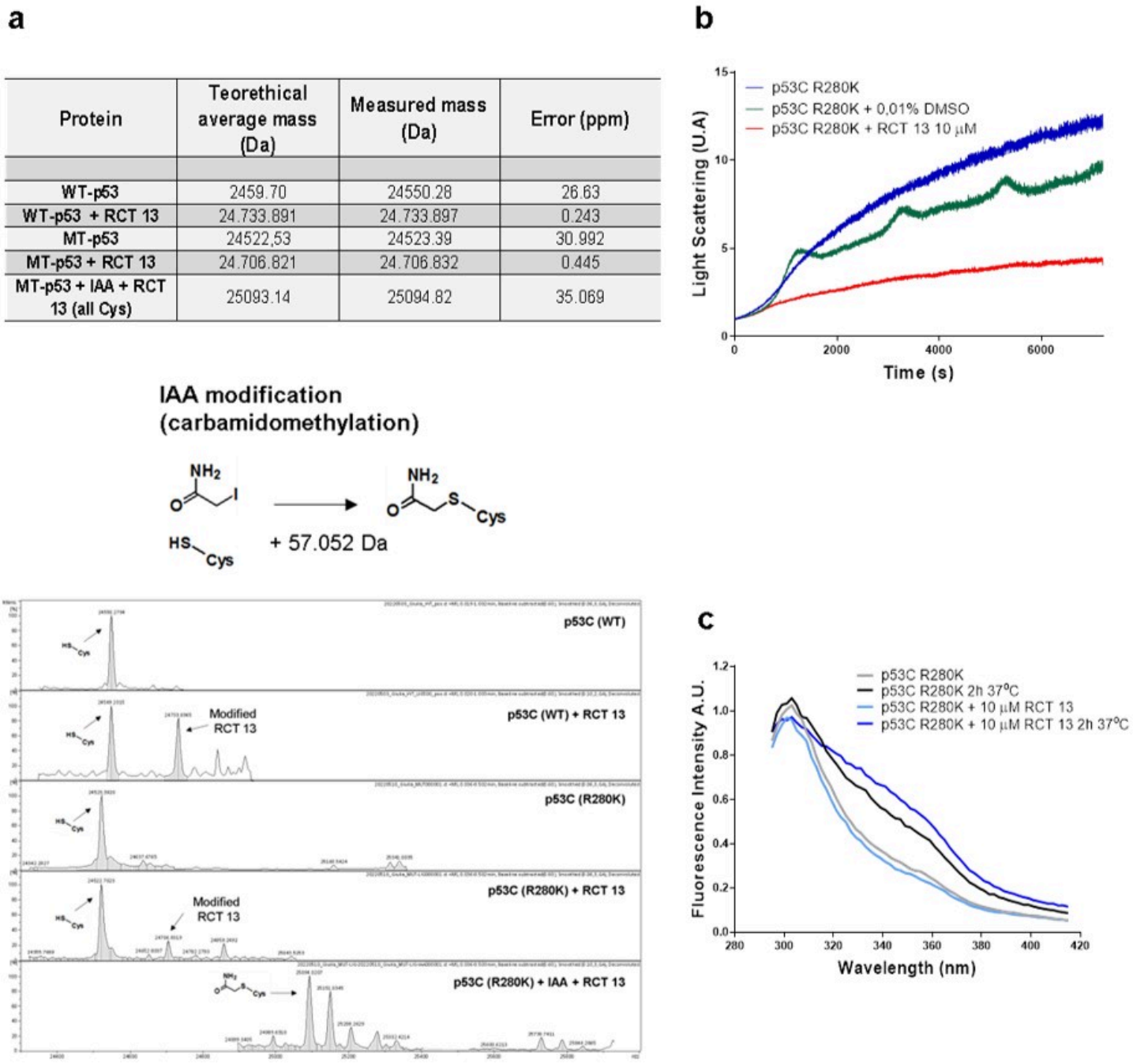


Figure 4

RCT-13 reduces mutant p53 aggregation in xenograft tumors in vivo. a, Representative confocal images of xenograft tumor sections stained with DO-1 (total p53) and A11 (amyloid-like aggregates). RCT-13–treated tumors show reduced DO-1/A11 colocalization relative to vehicle controls, indicating decreased p53 aggregation. Scale bar, 20 μm. b, Representative H&E staining of tumor and liver sections. RCT-13–treated tumors show reduced cellular density and invasion compared with controls. c, Liver sections

show preserved histological architecture, indicating the absence of detectable hepatotoxicity. Scale bar, 50 µm.



Protein	Teorethical average mass (Da)	Measured mass (Da)	Error (ppm)
WT-p53	2459.70	24550.28	26.63
WT-p53 + RCT 13	24.733.891	24.733.897	0.243
MT-p53	24522,53	24523.39	30.992
MT-p53 + RCT 13	24.706.821	24.706.832	0.445
MT-p53 + IAA + RCT 13 (all Cys)	25093.14	25094.82	35.069

Figure 5

RCT-13 covalently interacts with p53 R280K DBD and prevents its aggregation in vitro. a, Intact-protein mass spectrometry of purified WT or R280K p53 DBD before and after incubation with RCT-13. A mass shift consistent with covalent adduct formation is observed. Pre-alkylation with iodoacetamide prevents RCT-13 binding, confirming thiol-dependent reactivity. b, Light-scattering kinetics of purified R280K DBD (5 µM) at 37 °C for 2 h in the presence or absence of 10 µM RCT-13. RCT-13 markedly reduces scattering intensity, indicating potent inhibition of aggregation. c, Intrinsic fluorescence emission spectra of R280K

DBD before and after incubation with RCT-13, showing minimal spectral shift consistent with subtle conformational stabilization rather than unfolding. Data represent mean ± s.e.m. of n = 3 independent experiments.

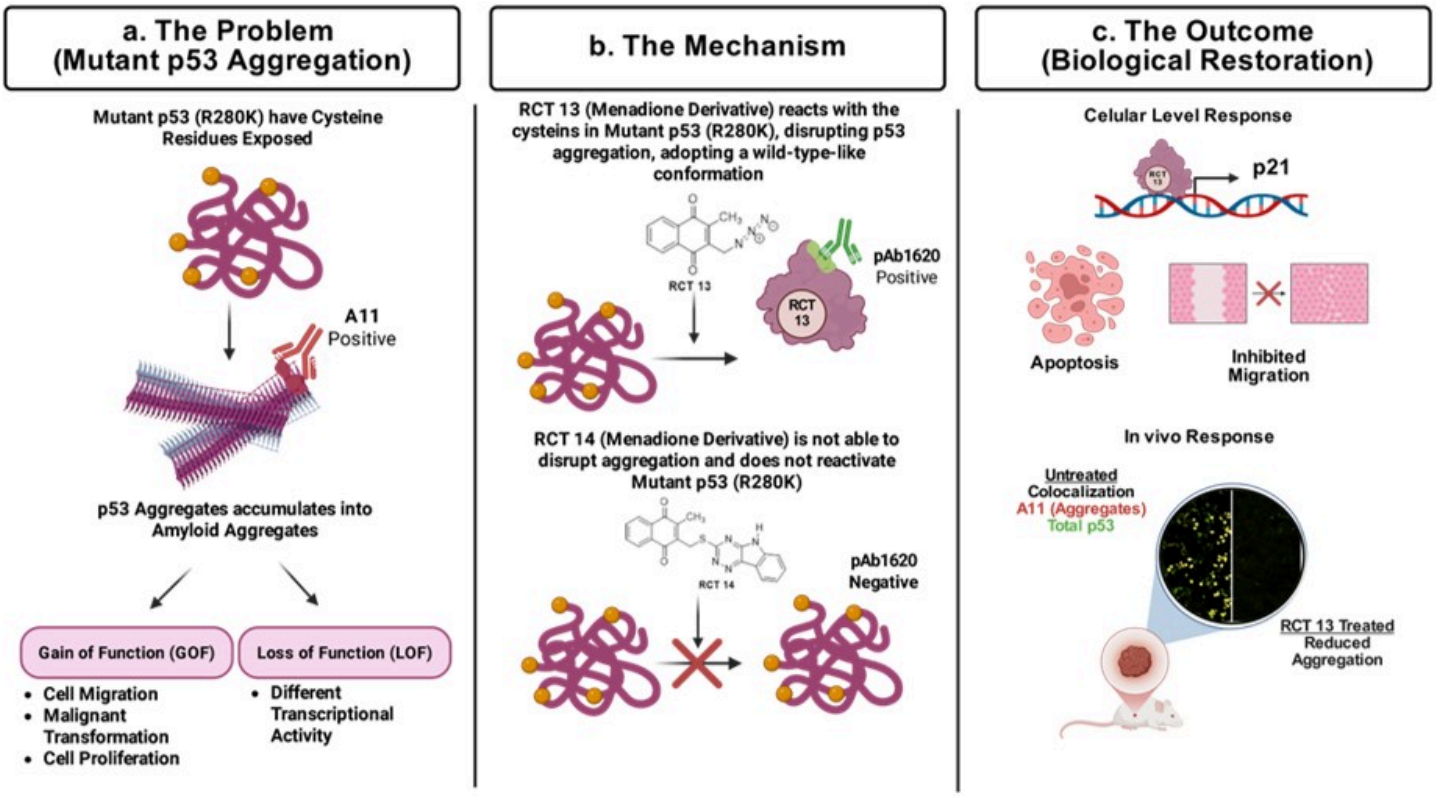


Figure 6

Covalent stabilization of mutant p53 by RCT-13 reverses amyloid aggregation and restores tumor suppression. a. The problem (mutant p53 aggregation). The p53 R280K mutation results in an unfolded protein with exposed cysteine residues that assembles into amyloid-like fibrils (A11 positive). This aggregation drives gain-of-function (GOF) phenotypes, such as migration and invasion, and causes loss of function (LOF) due to a lack of transcriptional activity. **b. The mechanism (covalent targeting).** RCT-13 covalently binds to exposed cysteines on the unfolded mutant p53, stabilizing it into a folded, wild-type-like conformation recognized by pAb1620. The inactive analog, RCT-14, fails to bind and does not prevent aggregation. **c. The outcome (biological restoration).** (*Top panel*) Refolded p53 restores DNA binding and transcriptional activation of target genes like *p21* (mRNA), inducing apoptosis and inhibiting cell migration. (*Bottom panel*) In tumor xenografts, RCT-13 treatment significantly reduces A11-positive aggregates (red) relative to total p53 (green) compared to untreated controls, leading to tumor cell death and structural vacuolization.

Supplementary Files

This is a list of supplementary files associated with this preprint. Click to download.

- SuplementaryInformationJersonSilva.docx